

Updated Air-Shower X_{\max} Moment Parametrizations for UHECR Composition with Latest Hadronic Interaction Models

Carmelo Evoli^{a,c}, Igor Vaiman^{a,c}, Sergio Petrer^{a,c}, Francesco Salamida^{b,c}

^aGran Sasso Science Institute (GSSI), Viale Francesco Crispi 7, L'Aquila, 67100, AQ, Italy

^bUniversità degli Studi dell'Aquila, Dipartimento di Scienze fisiche e chimiche Via Vetoio, L'Aquila, 67100, AQ, Italy

^cINFN-Laboratori Nazionali del Gran Sasso(LNGS), Via G. Acitelli 22, Assergi, 67100, AQ, Italy

Abstract

The mass composition of ultra-high-energy cosmic rays (UHECRs) is commonly inferred from the first two moments of the depth of shower maximum, X_{\max} , measured by fluorescence and hybrid detectors. Such analyses require fast and accurate mappings between the moments of X_{\max} and those of the logarithmic mass, $\ln A$, based on realistic air-shower simulations. In this work we provide updated parametrizations of the X_{\max} moments and distributions for air showers initiated by nuclei from proton to iron, simulated with CONEX for three state-of-the-art hadronic interaction models: EPOS-LHC, SIBYLL,2.3E, and QGSJET-III-01.

We parametrize the mean depth $\langle X_{\max} \rangle$ and the variance $\sigma^2(X_{\max})$ as functions of energy and mass. For the variance we compare a second-order polynomial model with an exponential model. In addition, we model the full X_{\max} distributions with a three-parameter generalized Gumbel function. The Gumbel parameters are fitted using an unbinned likelihood and are validated by comparing the implied mean and variance with the raw CONEX samples and with the moment parametrizations.

Across the full energy range considered, residuals between the parametrizations (or the Gumbel representation) and the simulations are at the level of a few g cm^{-2} for the mean and a few $(\text{g cm}^{-2})^2$ for the variance, making these parametrizations suitable for precision UHECR composition studies and forward-folding analyses of X_{\max} distributions.

Keywords: Cosmic-ray physics, UHECR, Hadronic Interaction Models

1. Introduction

The mass composition of ultra-high-energy cosmic rays (UHECRs) remains one of the central unknowns in astroparticle physics, with direct implications for the identification of their sources, acceleration mechanisms, and propagation effects. Among the shower observables accessible to current fluorescence and hybrid detectors, the most widely used composition-sensitive quantities are the mean depth of shower maximum, $\langle X_{\max} \rangle$, and its fluctuations, commonly expressed through the dispersion $\sigma(X_{\max})$. These observables provide a compact description of the longitudinal development of extensive air showers and can be related, in a statistical sense, to the mass and energy of the primary particle [1].

Interpreting $\langle X_{\max} \rangle$ and $\sigma(X_{\max})$ in terms of primary mass, however, unavoidably relies on air-shower simulations, and thus on the adopted hadronic interaction model (HIM). Modern HIMs are all tuned to reproduce collider data at accessible energies, but they differ in the physical

assumptions used to extrapolate multiparticle production, cross sections, and secondary spectra into the kinematic regime relevant for UHECR-induced interactions. As a consequence, the predicted $\langle X_{\max} \rangle$ and $\sigma(X_{\max})$ for a given primary mass can differ significantly among models [2]. Despite substantial progress in hadronic interaction modeling at ultra-high energies, air-shower physics beyond terrestrial accelerators still carries sizable and difficult-to-quantify systematic uncertainties (see, e.g., Ref. [3]), which propagate directly into composition inferences. The question of how to use X_{\max} information to constrain composition in the presence of hadronic-model uncertainties has motivated several dedicated studies, including early work based on moment parametrizations and their application to experimental data [2].

Over the past decade, continuous improvements in fluorescence reconstruction and atmospheric monitoring have enabled increasingly precise measurements of X_{\max} . The Pierre Auger Observatory reports systematic uncertainties on X_{\max} of order 10 g cm^{-2} [4], while the Telescope Array quotes $\pm 17 \text{ g cm}^{-2}$ [5]. That is why, in parallel with these experimental advances, recent composition studies increasingly exploit the *full* X_{\max} distribution rather than only its first two moments [6]. This shift places stringent requirements on the modeling of the distribution shape, because several steps in the analysis chain depend on an a priori description of the expected X_{\max} probability density. A widely adopted approach is to represent simulated X_{\max} distributions with Gumbel-type functions (see [7] and references therein), which have been shown to reproduce Monte Carlo predictions with high fidelity across relevant energy ranges and primary masses [8].

Reliable parametrizations of both the moments and the distribution shape therefore constitute an essential interface between air-shower simulations and experimental composition analyses.

The purpose of this paper is to provide an updated and self-consistent set of parametrizations for $\langle X_{\max} \rangle$, $\sigma(X_{\max})$, and the corresponding Gumbel description of the X_{\max} distribution, based on the latest developments in hadronic interaction modeling. By fitting the parametrizations to current HIM implementations, we aim to deliver a practical tool for ongoing and forthcoming UHECR composition studies, facilitating comparisons between experiments and improving the robustness of mass-inference procedures against model-dependent effects. We also compare X_{\max} observables' parametrization between latest and previous versions of each HIM, quantifying the impact of the update on observables and highlighting energy ranges where it is the largest.

2. CONEX simulations

Dedicated CONEX simulations of extensive air-shower development were performed using version 7.801¹. The X_{\max} distributions used for the fits were obtained for the following hadronic interaction models: Sibyll 2.3e [9], EPOS LHC-R [10], and QGSJet III-01 [11] (see Appendix A for a comparison with previous generations of these models). Simulations were carried out for primary nuclei H ($A = 1$), He ($A = 4$), N ($A = 14$), Si ($A = 28$), and Fe ($A = 56$). The datasets cover the energy range $\log_{10}(E/\text{eV}) = 17.5\text{--}20.5$, chosen to match the range used in mass-composition analyses of the Pierre Auger Observatory [6].

An extension of the simulations and parametrizations to heavier primaries and lower-energies is planned for a forthcoming paper.

Simulations are performed for 13 values of energy with step $\Delta \log_{10} E = 0.25$. For each energy, at least 10^4 showers were simulated. The zenith angle was fixed at 60° , and no significant dependence of the results on this choice was observed.

¹<https://gitlab.iap.kit.edu/AirShowerPhysics/cxroot/-/tree/conex2r7.801>

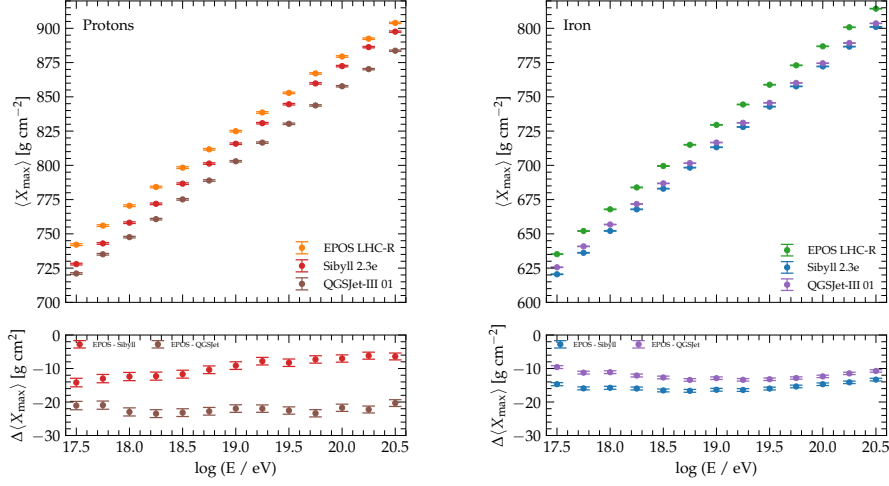


Figure 1: Mean X_{\max} as a function of energy for protons (left) and iron (right), as obtained for the three hadronic interaction models: Sibyll 2.3e, EPOS LHC-R, and QGSJet III-01. The lower panels display the systematic differences of Sibyll 2.3e and QGSJet III-01 with respect to EPOS LHC-R.

The X_{\max} values are taken from the $X_{\max}dE/dX$ branch of the CONEX output, which corresponds to a quadratic interpolation of the three highest $dE/dX(X_{\max})$ points.

For each energy bin we computed the mean and variance of X_{\max} over N simulated showers as follows:

- Mean and error of the mean:

$$\mu_X = \frac{1}{N} \sum_{i=1}^N X_i, \quad \delta\mu_X = \frac{\sigma_X}{\sqrt{N}}, \quad (1)$$

- Variance and error of the variance:

$$\sigma_X^2 = \frac{1}{N-1} \sum_{i=1}^N (X_i - \langle X \rangle)^2, \quad \delta\sigma_X^2 = \sigma_X^2 \sqrt{\frac{2}{N-1}}. \quad (2)$$

We present comparative plots of the mean $\mu_X = \langle X_{\max} \rangle$ and standard deviation $\sigma_X = \sqrt{\sigma^2(X_{\max})}$ for the three hadronic interaction models, focusing on the two extreme cases of primary mass: protons and iron nuclei (Figs. 1 and 2, respectively).

Across the full energy range considered, EPOS LHC-R predicts the deepest shower maxima for protons, followed by Sibyll 2.3e and QGSJet III-01. For iron primaries, this ordering changes: Sibyll 2.3e yields the shallowest X_{\max} , while EPOS LHC-R and QGSJet III-01 predict deeper shower maxima.

For the fluctuations, significant differences also emerge between models. In general, EPOS LHC-R predicts larger variances of X_{\max} , while QGSJet III-01 and Sibyll 2.3e lead to narrower distributions, especially for proton primaries. In the case of iron, the QGSJet III-01 predictions deviate significantly from those of the other two models, with direct implications for

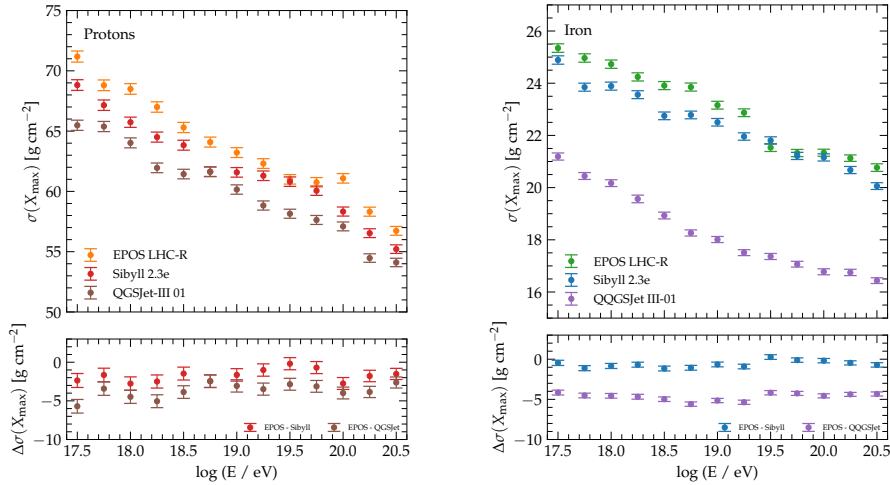


Figure 2: Standard deviation of X_{\max} as a function of energy for protons (left) and iron (right), as obtained for the three hadronic interaction models: Sibyll 2.3e, EPOS LHC-R, and QGSJet III-01. The lower panels display the systematic differences of Sibyll 2.3e and QGSJet III-01 with respect to EPOS LHC-R.

mass-composition inferences based on this model. Such comparisons are particularly relevant for assessing the systematic uncertainties associated with the choice of hadronic interaction model in mass-composition analyses.

3. X_{\max} parametrizations of mean and variance above $10^{17.5}$ eV

In this section we describe the functional forms adopted to parametrize the mean and variance of the X_{\max} distributions. The parametrizations are conveniently expressed in terms of two variables:

$$\epsilon \equiv \log_{10}(E/E_0), \quad Y \equiv \ln A, \quad (3)$$

where E is the primary energy, $E_0 = 10^{19}$ eV is a reference energy, and A is the mass number of the primary nucleus. To simplify notation, X_{\max} is also abbreviated as X throughout.

In the context of the so-called *superposition model* the mean depth of maximum is a function of the energy-per-nucleon, E/A . The dependence is commonly assumed to be linear in its logarithm, following the Heitler model [12]. In this paper we use a generalization of these models and, following [2], we use a parametrization with four free parameters (a_0, a_1, b_0, b_1):

$$\begin{aligned} a'(\epsilon) &= a_0 + a_1 \epsilon, \\ b'(\epsilon) &= b_0 + b_1 \epsilon, \\ \mu_X(\epsilon, Y) &= a'(\epsilon) + b'(\epsilon) Y. \end{aligned} \quad (4)$$

This expression separates the pure energy dependence, $a'(\epsilon)$, from the linear mass dependence encoded in $b'(\epsilon)Y$.

For the variance of the distributions we consider two alternative parametrizations. The first follows [2] and is based on a second-order polynomial dependence on ϵ and a quadratic expan-

sion in Y , for a total of six free parameters ($c_0, c_1, c_2, d_0, d_1, d_2$):

$$\begin{aligned} c'(\epsilon) &= c_0 + c_1 \epsilon + c_2 \epsilon^2, \\ d'(\epsilon) &= d_0 + d_1 \epsilon, \\ \sigma_X^2(\epsilon, Y) &= c'(\epsilon) [1 + d'(\epsilon) Y + d_2 Y^2]. \end{aligned} \quad (5)$$

The second parametrization is based on an exponential dependence on Y :

$$\begin{aligned} f'(\epsilon) &= f_0 + f_1 \epsilon, \\ g'(\epsilon) &= g_0 + g_1 \epsilon, \\ \sigma_X^2(\epsilon, Y) &= \exp[f'(\epsilon) + g'(\epsilon) Y]. \end{aligned} \quad (6)$$

This form guarantees $\sigma_X^2 > 0$ for all ϵ and Y and introduces four free parameters (f_0, f_1, g_0, g_1).

The first parametrization, Eq. (5), has the advantage of leading to a simple analytical inversion when mapping $\sigma_{X_{\max}}^2$ to $\sigma_{\ln A}^2$ in composition analyses. However, its polynomial dependence on Y can lead to an unphysical upturn of σ_X^2 outside the validity range in mass, due to the quadratic term in Y .

The exponential parametrization, Eq. (6), typically yields smaller residuals with respect to the simulated variances and can be more robust when extrapolated to higher masses, even though the inversion from $\sigma_{X_{\max}}^2$ to $\sigma_{\ln A}^2$ is less simple (see also [13]). All these aspects will be treated in more details in Sec. 4.

3.1. Fit parameters

The best-fit values of the parameters for each hadronic interaction model are reported in Table B.1 for μ_X and σ_X^2 , respectively. These values were obtained by fitting the statistics of the CONEX simulation datasets introduced in Section 2.

The fits were performed with the `iminuit` [14] minimization package, using the standard MIGRAD χ^2 minimization. The reduced χ^2 values (χ^2/ndf) corresponding to the best-fit parameters are listed in the last column of the table.

The χ^2 is computed using, as uncertainties, the statistical errors on the mean and variance as defined in Section 2. For this reason, the absolute χ^2 values should not be interpreted as a measure of the overall goodness-of-fit, but rather as a relative indicator to compare the quality of the fits among different hadronic interaction models.

To validate the parametrizations, we compare them directly with the results of the CONEX simulations. Figure 3 shows, for representative primary nuclei, the simulated values of μ_X and σ_X together with the corresponding analytical parametrizations. In the lower panels of each figure we report the residuals, defined as the absolute difference between the simulation result and the parametrization:

$$\Delta(F) = |F_{\text{CONEX}} - F_{\text{parametrization}}|. \quad (7)$$

This representation gauges the accuracy of the fits across the full energy range. In addition to the graphical comparisons, we provide a quantitative summary of the residuals. For each hadronic interaction model and primary species, we compute the average residual in the energy range $E \geq 10^{17.5}$ eV. These values are reported in Tables B.3 and B.4, for $\langle X_{\max} \rangle$ and $\sigma(X_{\max})$, respectively.

The average residuals for $\langle X_{\max} \rangle$ are found to be small, typically at the level of 1–2 g cm⁻², confirming that the parametrizations reproduce the simulation results with high accuracy across the range relevant for composition studies.

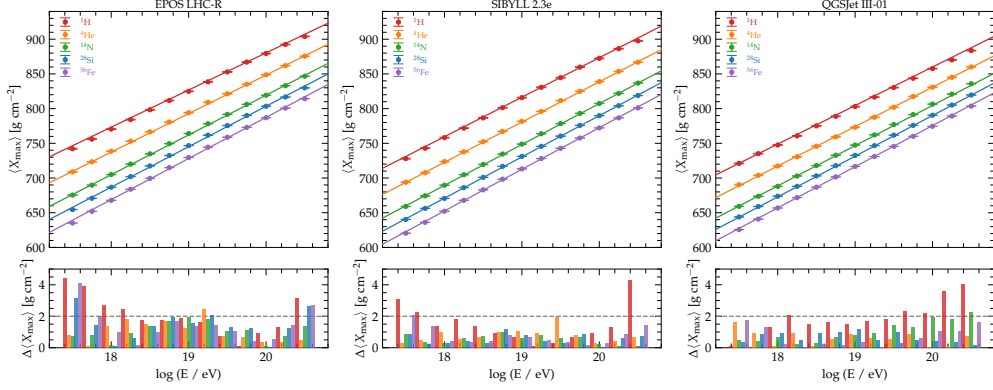


Figure 3: Comparison between the parametrizations and the CONEX simulations for $\langle X_{\max} \rangle$ for the three hadronic interaction models: EPOS LHC-R (left), Sibyll 2.3e (middle), and QGSJet III-01 (right). The upper panels show the simulated values (dots) together with the analytical parametrizations (solid lines) for representative primary nuclei. The lower panels display the residuals, defined as in Eq. 7.

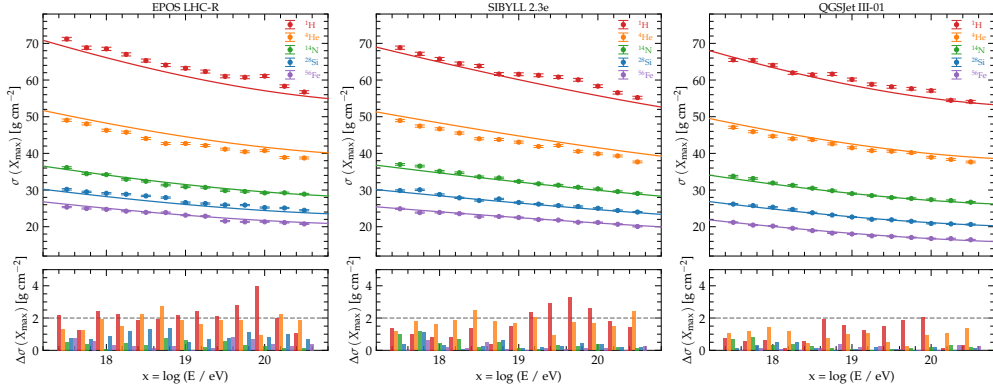


Figure 4: Same as Fig. 3, but for $\sigma(X_{\max})$ using the second-order polynomial parametrization of Eq. 5.

The standard deviation, on the other hand, exhibits a systematic bias of about $1\text{--}2 \text{ g cm}^{-2}$ for protons and helium across the entire energy range when using the second-order polynomial model in Eq. (5), corresponding to a relative difference of roughly 3–4%. Employing exponential functions, as in the model of Eq. (6), reduces the bias to below 2% for EPOS LHC-R and Sibyll 2.3e, while it slightly worsens the bias in the case of QGSJet III-01. However, we stress that adopting the second-order polynomial functional form preserves the analytical invertibility of the relation, which is required to derive $\ln A$ from the measurement of $\sigma(X_{\max})$, as discussed in Sec. 2 of [2] and in Sec. 4.

4. Mapping between X_{\max} moments and $\ln A$ moments

In composition analyses, it is customary to characterize the X_{\max} distribution at fixed energy by its first two moments: the mean $\langle X_{\max} \rangle$ and the variance $\sigma^2(X_{\max})$. When adopting the model-dependent parameterizations introduced in Sec. 3, it is often more convenient to express the

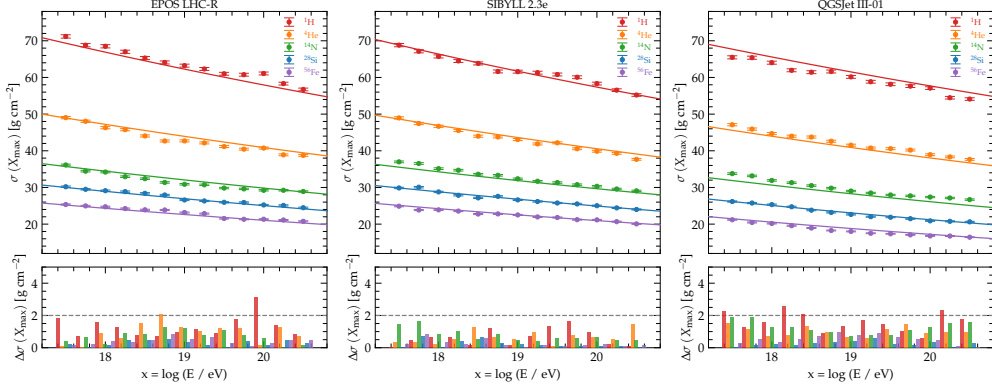


Figure 5: Same as Fig. 3, but for $\sigma(X_{\max})$ using the exponential parametrization of Eq. 6.

composition in terms of the mean logarithmic mass and its variance. The mean logarithmic mass follows directly from Eq. (4). For greater transparency and ease of interpretation, we rewrite this relation as in [2]

$$\langle X_{\max} \rangle_Y = X_p(\epsilon) + f_E(\epsilon) Y, \quad (8)$$

where $X_p = a'(\epsilon)$ denotes the proton $\langle X_{\max} \rangle$, and $f_E = b'(\epsilon)$ is the (energy-dependent) slope relating shifts in $\ln A$ to shifts in X_{\max} . Averaging over the mass distribution yields

$$\langle X_{\max} \rangle = X_p(\epsilon) + f_E(\epsilon) \langle Y \rangle \quad \implies \quad \langle Y \rangle = \frac{\langle X_{\max} \rangle - X_p(\epsilon)}{f_E(\epsilon)}. \quad (9)$$

In the case of a single mass having logarithmic value Y , the variance of X_{\max} is entirely determined by intrinsic shower-to-shower fluctuations, so that

$$\sigma_X^2(\epsilon, Y) = \sigma_{\text{sh}}^2(\epsilon, Y).$$

For mixed mass compositions, however, the total variance receives contributions from both intrinsic shower fluctuations and mass mixing. Applying the law of total variance, one obtains

$$\sigma_X^2(\epsilon, \langle Y \rangle) = \langle \sigma_{\text{sh}}^2(\epsilon, Y) \rangle + f_E^2(\epsilon) \sigma_Y^2. \quad (10)$$

Equation (9) provides a direct mapping between $\langle X_{\max} \rangle$ and $\langle \ln A \rangle$, while Eq. (10) relates the measured variance of X_{\max} to the mass dispersion $\sigma^2(\ln A)$ once a model for $\sigma_{\text{sh}}^2(\epsilon, Y)$ is specified.

Quadratic model for intrinsic fluctuations. In [2] it is proposed to model the intrinsic variance as a quadratic function of Y , as given by (5)

$$\sigma_{\text{sh}}^2(\epsilon, Y) = \sigma_p^2(\epsilon) \left[1 + d'(\epsilon) Y + d_2 Y^2 \right], \quad (11)$$

where the parameter c' has been replaced by σ_p^2 in order to highlight its physical meaning as the intrinsic shower-to-shower fluctuations for protons.

Using $\langle Y^2 \rangle = \langle Y \rangle^2 + \sigma_Y^2$, Eq. (10) becomes

$$\sigma_X^2 = \sigma_p^2 \left[1 + d'(\epsilon) \langle Y \rangle + d_2 \langle Y \rangle^2 \right] + (d_2 \sigma_p^2 + f_E^2) \sigma_Y^2. \quad (12)$$

Replacing the first addendum with $\sigma_{\text{sh}}^2(\epsilon, \langle Y \rangle)$, which represents the fluctuations associated with a logarithmic mass $\langle Y \rangle$, one finally gets

$$\sigma_Y^2 = \frac{\sigma_X^2 - \sigma_{\text{sh}}^2(\epsilon, \langle Y \rangle)}{d_2 \sigma_p^2 + f_E^2}. \quad (13)$$

Exponential model for intrinsic fluctuations. In the present work we also consider an alternative description of the intrinsic fluctuations, in which the shower variance depends exponentially on Y , as in (6)

$$\sigma_{\text{sh}}^2(\epsilon, Y) = \exp[f'(\epsilon) + g'(\epsilon) Y]. \quad (14)$$

In this case Eq. (10) becomes

$$\sigma_X^2 = \left\langle \exp[f'(\epsilon) + g'(\epsilon) Y] \right\rangle + f_E^2(\epsilon) \sigma_Y^2. \quad (15)$$

The average of the exponential function depends on the probability distribution function of Y , $p(Y)$. In our case, this function is unknown, but its first two moments $\langle Y \rangle$ and σ_Y^2 are precisely the quantities we wish to infer. A natural choice is therefore to approximate $p(Y)$ by a Gaussian

$$p(Y) \simeq \mathcal{N}(Y; \langle Y \rangle, \sigma_Y^2), \quad (16)$$

which is fully determined by those two moments. Under this assumption one obtains

$$\left\langle \exp(f' + g'Y) \right\rangle = \exp[f' + g'\langle Y \rangle] \exp\left(\frac{1}{2}g'^2 \sigma_Y^2\right), \quad (17)$$

where, for compactness, we have omitted the explicit dependence on ϵ .

Inserting Eq. (17) into Eq. (15) leads to the implicit equation

$$\sigma_X^2 - \sigma_{\text{sh}}^2(\epsilon, \langle Y \rangle) \exp\left(\frac{1}{2}g'^2 \sigma_Y^2\right) - f_E^2 \sigma_Y^2 = 0, \quad (18)$$

to be solved for σ_Y^2 . Unlike the quadratic case, σ_Y^2 now appears both linearly and in the exponent, so the inversion is no longer a simple algebraic expression. In practice, Eq. (18) can be solved numerically with standard root-finding algorithms.

Eq. (18) can also be solved in closed form using the Lambert W function as

$$\sigma_Y^2 = \frac{\sigma_X^2}{f_E^2} - \frac{2}{g'^2} W_0\left(\frac{g'^2}{2f_E^2} \sigma_{\text{sh}}^2(\epsilon, \langle Y \rangle) \exp\left[\frac{g'^2}{2f_E^2} \sigma_X^2\right]\right), \quad (19)$$

where W_0 is the principal branch of the Lambert W function.

Given these ingredients, the exponential model provides a consistent forward description of $\sigma_{\text{sh}}^2(\epsilon, Y)$ and, via Eq. (18) (or Eq. (19)), an in-principle invertible mapping between the measured X_{max} moments and the underlying $\ln A$ moments.

5. Parameterization of X_{max} distributions

Beyond the first two moments, a full description of the X_{max} distributions is required for composition analyses that exploit the full shape of the profiles. Following the approach introduced in Ref. [7], we model the simulated X_{max} distributions with generalized Gumbel functions. This

method has been extensively used in combined fits of the energy spectrum and mass composition of UHECR measurements (see e.g. [15, 16]) and provides a compact analytical representation of the distributions for all hadronic interaction models considered in this work.

The functional form of the generalized Gumbel distribution is

$$\mathcal{G}(X; \mu, \sigma, \lambda) = \frac{1}{\sigma} \frac{\lambda^\lambda}{\Gamma(\lambda)} \exp[-\lambda(z + e^{-z})], \quad z \equiv \frac{X - \mu}{\sigma}, \quad (20)$$

with $\sigma > 0$ and $\lambda > 0$. Here μ is the location parameter, σ the scale, and λ a shape parameter controlling the skewness of the distribution. For $\lambda = 1$, Eq. (20) reduces to the standard (type-I) Gumbel distribution. This parametrization has been shown to perform better than other proposed functional forms in reproducing both the asymmetric shape and the tail behaviour of the X_{\max} distributions [8].

Each of the Gumbel parameters is expressed as a smooth function of the logarithmic energy $\epsilon \equiv \log_{10}(E/E_0)$, with $E_0 = 10^{19}$ eV, and of the logarithm of the mass number $Y \equiv \ln A$. In particular, the location parameter μ is modeled as a quadratic function of ϵ , with coefficients that are themselves quadratic functions of Y . The scale σ and shape λ parameters are modeled as linear functions of ϵ , again with Y -dependent quadratic coefficients. Explicitly:

- Location $\mu(\epsilon, Y)$ (quadratic in ϵ):

$$\begin{aligned} p_0^\mu(Y) &= a_0^\mu + a_1^\mu Y + a_2^\mu Y^2, \\ p_1^\mu(Y) &= b_0^\mu + b_1^\mu Y + b_2^\mu Y^2, \\ p_2^\mu(Y) &= c_0^\mu + c_1^\mu Y + c_2^\mu Y^2, \\ \mu(\epsilon, Y) &= p_0^\mu(Y) + p_1^\mu(Y) \epsilon + p_2^\mu(Y) \epsilon^2. \end{aligned} \quad (21)$$

- Scale $\sigma(\epsilon, Y)$ (linear in ϵ):

$$\begin{aligned} p_0^\sigma(Y) &= a_0^\sigma + a_1^\sigma Y + a_2^\sigma Y^2, \\ p_1^\sigma(Y) &= b_0^\sigma + b_1^\sigma Y + b_2^\sigma Y^2, \\ \sigma(\epsilon, Y) &= p_0^\sigma(Y) + p_1^\sigma(Y) \epsilon. \end{aligned} \quad (22)$$

- Shape $\lambda(\epsilon, Y)$ (linear in ϵ):

$$\begin{aligned} p_0^\lambda(Y) &= a_0^\lambda + a_1^\lambda Y + a_2^\lambda Y^2, \\ p_1^\lambda(Y) &= b_0^\lambda + b_1^\lambda Y + b_2^\lambda Y^2, \\ \lambda(\epsilon, Y) &= p_0^\lambda(Y) + p_1^\lambda(Y) \epsilon. \end{aligned} \quad (23)$$

In total, this scheme involves 9 coefficients for μ , and 6 coefficients each for σ and λ , yielding 21 free parameters.

To determine these coefficients, we perform a global unbinned maximum-likelihood fit to the full set of simulated X_{\max} values for each hadronic interaction model. Each simulated shower is characterized by its energy E_i , mass number A_i and depth of shower maximum $X_{\max,i}$, from which we construct $\epsilon_i \equiv \log_{10}(E_i/E_0)$, and $Y_i \equiv \ln A_i$.

For given values of the parameter vector θ , containing the 21 polynomial coefficients entering Eqs. (21)–(23), we compute the corresponding Gumbel parameters $\mu_i \equiv \mu(\epsilon_i, Y_i; \theta)$, $\sigma_i \equiv$

$\sigma(\epsilon_i, Y_i; \boldsymbol{\theta})$ and $\lambda_i \equiv \lambda(\epsilon_i, Y_i; \boldsymbol{\theta})$ for each event i . Assuming independent showers, the likelihood for the full data set $\{X_{\max,i}\}_{i=1}^N$ is

$$\mathcal{L}(\boldsymbol{\theta}) = \prod_{i=1}^N \mathcal{G}[X_{\max,i}; \mu_i(\epsilon_i, Y_i; \boldsymbol{\theta}), \sigma_i(\epsilon_i, Y_i; \boldsymbol{\theta}), \lambda_i(\epsilon_i, Y_i; \boldsymbol{\theta})], \quad (24)$$

and we maximize the corresponding log-likelihood (for compactness, we omit the explicit dependence of $\mu_i, \sigma_i, \lambda_i$ on $\epsilon_i, Y_i, \boldsymbol{\theta}$)

$$\ln \mathcal{L}(\boldsymbol{\theta}) = \sum_{i=1}^N \ln \mathcal{G}(X_{\max,i}; \mu_i, \sigma_i, \lambda_i). \quad (25)$$

Using the explicit form of the generalized Gumbel density in Eq. (20), the log-likelihood contribution of a single event i can be written as

$$\ln \mathcal{G}_i = -\ln \sigma_i + \lambda_i \ln \lambda_i - \ln \Gamma(\lambda_i) - \lambda_i z_i - \lambda_i e^{-z_i}, \quad z_i \equiv \frac{X_{\max,i} - \mu_i}{\sigma_i}. \quad (26)$$

It is numerically convenient to minimize the negative log-likelihood $\text{NLL}(\boldsymbol{\theta}) \equiv -\ln \mathcal{L}(\boldsymbol{\theta})$, which becomes

$$\text{NLL}(\boldsymbol{\theta}) = \sum_{i=1}^N \left[\ln \sigma_i - \lambda_i \ln \lambda_i + \ln \Gamma(\lambda_i) + \lambda_i z_i + \lambda_i e^{-z_i} \right]. \quad (27)$$

In the numerical implementation, μ_i, σ_i and λ_i are computed event by event from the polynomial parameterizations in ϵ_i and Y_i , and the sum in Eq. (27) is evaluated over all simulated showers. In this way, all available simulated events contribute directly to the determination of $\boldsymbol{\theta}$ without any loss of information from binning in X_{\max} .

5.1. Fit parameters

The coefficients entering Eqs. (21)–(23) are obtained by minimizing the negative log-likelihood in Eq. (27) for each hadronic interaction model. The minimization is performed with the `iminuit` [14] package, using the default `MIGRAD` algorithm, followed by a `HESSE` step to estimate the covariance matrix and the corresponding parameter uncertainties.

To ensure that the fit remains in a physically meaningful region of parameter space, we impose constraints on the Gumbel parameters implied by a given choice of $\boldsymbol{\theta}$. In particular, we require the scale and shape parameters to satisfy $\sigma_i > 0$ and $\lambda_i > 0$ for all events, and we restrict the dynamically computed values of μ_i, σ_i and λ_i to lie within broad but physically motivated intervals, $300 < \mu_i < 1300$, $10 < \sigma_i < 100$, and $0.01 < \lambda_i < 10$. Trial parameter sets that violate any of these conditions are assigned a very large value of NLL , so that they are effectively excluded from the region explored by the minimizer. Since Eq. (20) defines a properly normalized probability density, no additional free normalization parameter is introduced in the likelihood.

To mitigate possible dependence on the starting point of the minimization and reduce the risk of converging to local minima, we repeat the fit $N_{\text{seed}} = 100$ times with randomly chosen initial values of $\boldsymbol{\theta}$, sampled within wide ranges around physically reasonable expectations. For each seed, the minimization is iterated until `MIGRAD` converges and the `HESSE` matrix is successfully computed. Among all successful fits, we select as our best solution the one with the smallest deviance,

$$D(\boldsymbol{\theta}) \equiv -2 \ln \mathcal{L}(\boldsymbol{\theta}), \quad (28)$$

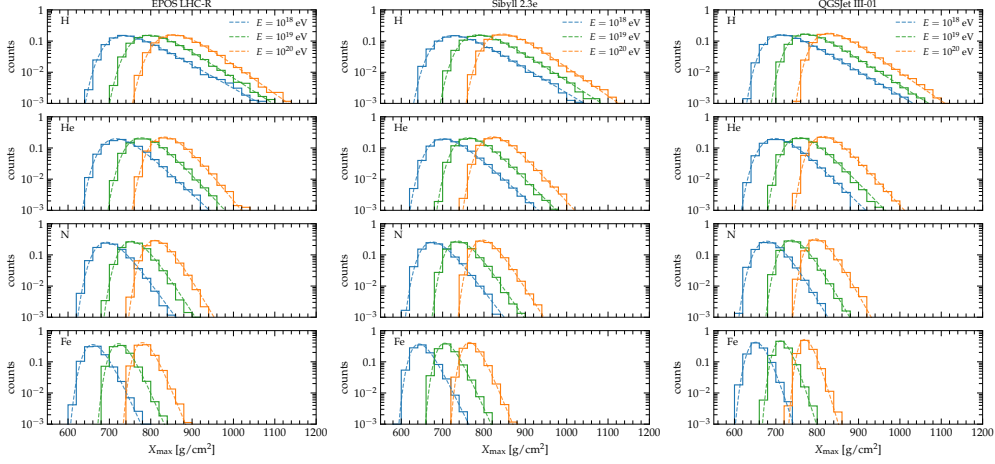


Figure 6: Representative examples of simulated X_{\max} distributions from CONEX (histograms) and the corresponding generalized Gumbel descriptions (solid curves) obtained from the global parameterization of Eqs. (21)–(23). From left to right, the panels refer to the hadronic interaction models EPOS LHC-R, Sibyll 2.3e, and QGSJet III-01. Each panel shows selected primaries (H, He, N, Fe) and energies (10^{18} eV, 10^{19} eV, 10^{20} eV) to illustrate the quality of the description across the simulated phase space.

which is equivalent to choosing the minimum of the negative log-likelihood up to an irrelevant additive constant.

The best-fit coefficients for the three hadronic interaction models (Sibyll 2.3e, EPOS LHC-R, QGSJet III-01) are reported in Table B.5. Representative examples of one-dimensional X_{\max} distributions for different primaries and energies are shown in Fig. 6, together with the corresponding generalized Gumbel functions evaluated using the global parameterization.

As an additional validation, we compare the cumulative distribution functions (CDFs) obtained from the CONEX simulations with those predicted by the Gumbel parameterization. Specifically, for H and Fe primaries at $E = 10^{18}$ eV and $E = 10^{20}$ eV, Fig. 7 displays the empirical CDFs, constructed directly from the ordered X_{\max} values, together with the theoretical CDFs obtained by integrating Eq. (20) from 0 to X . The lower panels show the residuals, defined as the difference between the simulated and fitted CDFs. These residuals remain at the few-percent level across the full range of X_{\max} , demonstrating that the generalized Gumbel parameterization provides a robust analytical representation of the X_{\max} distributions and is sufficiently accurate for use in combined spectrum and composition analyses.

6. Consistency of Gumbel representation

As an internal consistency check of the generalized Gumbel parameterization, we verify that the first two moments implied by the fitted Gumbel parameters reproduce the mean and variance of the underlying CONEX samples. For each (E, A) bin, the generalized Gumbel distribution in Eq. (20) has an analytical mean and variance given by

$$\langle X_{\max} \rangle_{\mathcal{G}} = \mu + \sigma [\ln \lambda - \psi(\lambda)], \quad (29)$$

$$\text{Var}(X_{\max})_{\mathcal{G}} = \sigma^2 \psi_1(\lambda), \quad (30)$$

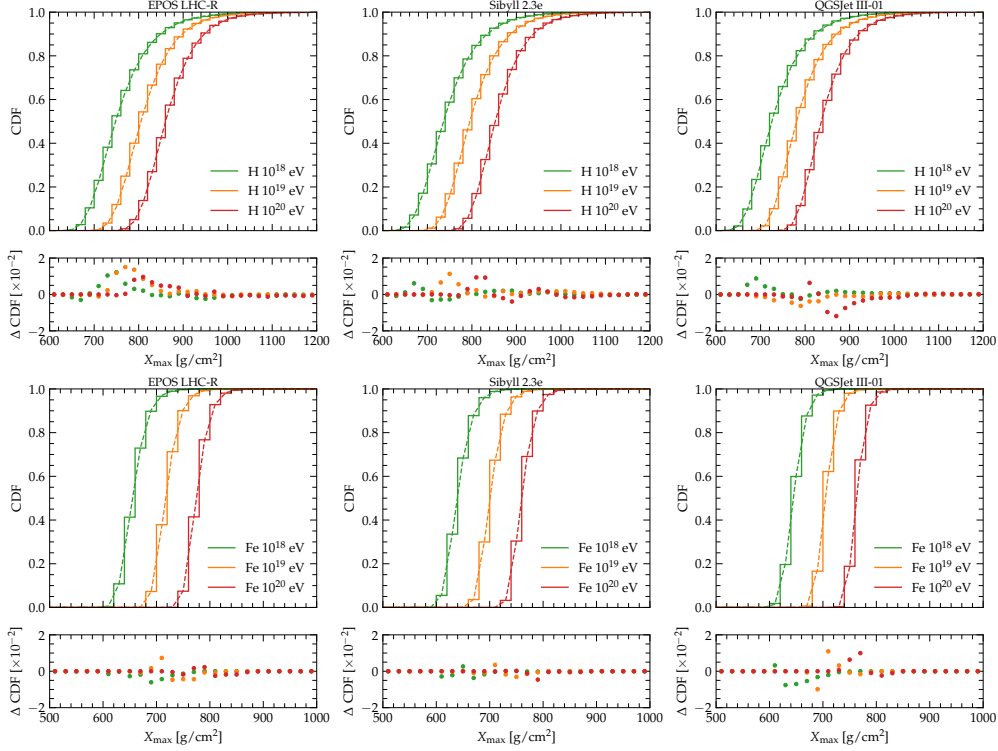


Figure 7: Empirical cumulative distribution functions (CDFs) of X_{\max} from CONEX simulations (histograms) compared to the CDFs predicted by the generalized Gumbel parameterization (solid lines) for H (top row) and Fe (bottom row). In each panel the three energies $E = 10^{18}$ eV, $E = 10^{19}$ eV and $E = 10^{20}$ eV are shown. Columns correspond, from left to right, to the hadronic interaction models EPOS LHC-R, Sibyll 2.3e, and QGSJet III-01. The lower sub-panels display the residuals $\Delta\text{CDF}(X) \equiv \text{CDF}_{\text{MC}}(X) - \text{CDF}_{\text{G}}(X)$.

where $\psi(\lambda)$ is the digamma function and $\psi_1(\lambda)$ is the trigamma function, i.e. the first derivative of $\psi(\lambda)$ with respect to λ . In our implementation, Eqs. (29)–(30) are evaluated using the fitted values of $\mu(\epsilon, Y)$, $\sigma(\epsilon, Y)$ and $\lambda(\epsilon, Y)$ from Eqs. (21)–(23) at the corresponding $\epsilon = \log_{10}(E/E_0)$ and $Y = \ln A$.

For each hadronic interaction model and for each (E, A) point on the simulation grid, we compute: (i) the sample mean and variance of X_{\max} directly from the CONEX showers, $\langle X_{\max} \rangle_{\text{MC}}$ and $\text{Var}(X_{\max})_{\text{MC}}$; (ii) the Gumbel-based moments $\langle X_{\max} \rangle_{\text{G}}$ and $\text{Var}(X_{\max})_{\text{G}}$ via Eqs. (29)–(30); and (iii) the moments obtained from the dedicated parameterizations of the first two moments introduced in Sec. 3. The corresponding biases are quantified using the definition in Eq. (7), applied separately to the mean and to the standard deviation.

The comparison is summarized in Figs 8 and 9, which shows the residuals between the CONEX moments and those obtained from the Gumbel representation, together with the residuals from the direct moment parameterizations, as a function of energy for representative primaries. Over the full range of energies and masses considered, the Gumbel-based moments track the CONEX results at the level of a few g cm^{-2} for the mean and a few percent for the variance, with no significant systematic trend as a function of E or A . The size and structure of the residuals are

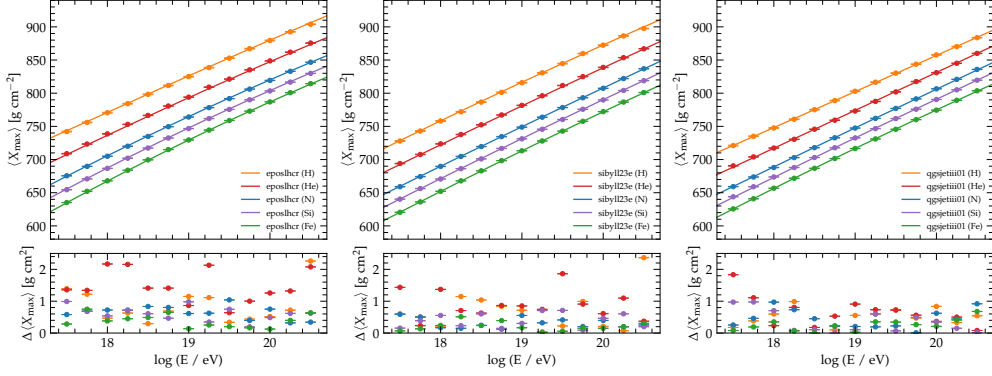


Figure 8: Mean depth of shower maximum, $\langle X_{\max} \rangle$, as a function of energy for representative primaries. Upper panels: CONEX sample means (points) compared to the prediction from the generalized Gumbel parameterization (solid lines), computed via Eq. (29). Lower panels: residuals defined as $\Delta \langle X_{\max} \rangle \equiv \langle X_{\max} \rangle_{\text{MC}} - \langle X_{\max} \rangle_{\text{G}}$. From left to right: EPOS LHC-R, Sibyll 2.3e, and QGSJet III-01.

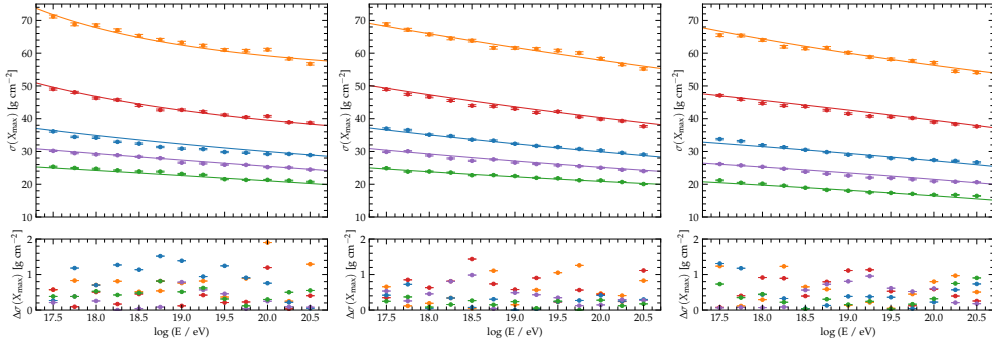


Figure 9: Same as Fig. 8, but for the X_{\max} standard deviation. Upper panels: $\text{Var}(X_{\max})$ from CONEX (points) compared to the generalized Gumbel prediction (solid lines), computed via Eq. (30). Lower panels: residuals $\Delta \text{Var}(X_{\max}) \equiv \text{Var}(X_{\max})_{\text{MC}} - \text{Var}(X_{\max})_{\text{G}}$. From left to right: EPOS LHC-R, Sibyll 2.3e, and QGSJet III-01.

comparable to those obtained with the dedicated moment parameterizations.

We therefore conclude that the generalized Gumbel parameterization provides a faithful and internally consistent description of the X_{\max} distributions: it not only reproduces the detailed histogram shapes and cumulative distributions, but also yields first and second moments that are fully consistent with those from the underlying CONEX simulations within the accuracy required for combined spectrum and composition analyses.

7. Conclusions

We have presented updated parametrizations of the first two moments of the depth of shower maximum, X_{\max} , and of the full X_{\max} distributions for ultra-high-energy cosmic-ray air showers. Using CONEX simulations for primary nuclei from proton to iron and three modern hadronic interaction models (Sibyll 2.3e, EPOS LHC-R, and QGSJet III-01), we derived compact descriptions of $\langle X_{\max} \rangle$ and $\sigma^2(X_{\max})$ as functions of energy and mass. For the variance, we explored

both a second-order polynomial and an exponential model: the polynomial form provides fully analytic forward and inverse mappings between the X_{\max} moments and the corresponding $\langle \ln A \rangle$ and $\text{Var}(\ln A)$, while the exponential case can be inverted numerically following the procedure described in this work.

In addition, we showed that the full X_{\max} distributions are well captured by a three-parameter generalized Gumbel function, with parameters obtained from unbinned likelihood fits. The resulting representation reproduces the simulated mean and variance with residuals at the level of a few g cm^{-2} and a few $(\text{g cm}^{-2})^2$, respectively, across the full energy range considered. These parametrizations therefore provide a practical interface between air-shower simulations and composition analyses, enabling efficient forward-folding studies and systematic comparisons across hadronic interaction models.

All the data products associated with this note are made publicly available through a dedicated Zenodo repository [17] while CONEX simulations are available upon request.

The released material includes the fitting parameters of derived parameterizations, in plain-text format for ease of use. Each file is provided separately for the three hadronic interaction models (Sibyll 2.3e, EPOS LHC-R, and QGSJet III-01). Below we summarize the available files and their content.

- `conex_*.xmax`: Tables of X_{\max} moments directly extracted from the CONEX simulations. For each hadronic interaction model and primary nucleus, the file reports the mean $\langle X_{\max} \rangle$ and its statistical uncertainty, as well as the variance $\sigma^2(X_{\max})$ and its uncertainty, as functions of energy. Units are g cm^{-2} and $\text{g}^2 \text{cm}^{-4}$, respectively.
- `conex_*.hist`: Binned X_{\max} distributions from the CONEX simulations. Each file covers the range $X_{\max} \in [0, 2000] \text{ g cm}^{-2}$, divided into $N = 100$ bins of width $\Delta X_{\max} = 20 \text{ g cm}^{-2}$. The entries are raw counts per bin (i.e. unnormalized histograms).
- `xmax_mean*_EVPS2026.txt`: Best-fit coefficients of the parametrization for the mean X_{\max} (Eq. 4). The file format is: (i) first row: best-fit parameters (a_0, a_1, b_0, b_1) ; (ii) second row: corresponding parameter uncertainties; (iii) third row: χ^2 and the number of degrees of freedom (ndf).
- `xmax_sigma2*_EVPS2026.txt`: Best-fit coefficients of the parametrization for the variance $\sigma^2(X_{\max})$ (Eq. 5). An additional keyword in the filename specifies the chosen functional form for σ^2 (e.g. `pol2` or `exp`). The file format is: (i) first row: best-fit parameters, $(c_0, c_1, c_2, d_0, d_1, d_2)$ for the polynomial model, or (f_0, f_1, g_0, g_1) for the exponential model; (ii) second row: corresponding parameter uncertainties; (iii) third row: χ^2 and ndf.
- `gumbel_params*_EVPS2026.txt`: Best-fit coefficients of the generalized Gumbel parametrization of the full X_{\max} distributions (Sec. 5). For each hadronic interaction model, the file reports the 21 coefficients entering the parametrizations of the three Gumbel parameters (μ, β, λ) , denoted as $p_k^{(i)}$ with $i \in \{\mu, \beta, \lambda\}$ and $k = 0, \dots, 2$.

These resources are intended to facilitate the direct use of the new parametrizations in composition analyses, and to support transparent cross-checks and systematic studies of hadronic-model dependencies.

Acknowledgements

We thank Denise Boncioli, Fabio Convegna, Alexey Yushkov, and Michael Unger for fruitful discussions and helpful comments on this work.

References

- [1] K.-H. Kampert, M. Unger, Measurements of the Cosmic Ray Composition with Air Shower Experiments, *Astropart. Phys.* 35 (2012) 660–678. [arXiv:1201.0018](#), [doi:10.1016/j.astropartphys.2012.02.004](#).
- [2] P. Abreu, et al., Interpretation of the Depths of Maximum of Extensive Air Showers Measured by the Pierre Auger Observatory, *JCAP* 02 (2013) 026. [arXiv:1301.6637](#), [doi:10.1088/1475-7516/2013/02/026](#).
- [3] J. Albrecht, et al., Road map for the tuning of hadronic interaction models with accelerator-based and astroparticle data (8 2025). [arXiv:2508.21796](#), [doi:10.1038/s42254-025-00897-3](#).
- [4] A. Abdul Halim, et al., Measurement of the depth of maximum of air-shower profiles with energies between 1018.5 and 1020 eV using the surface detector of the Pierre Auger Observatory and deep learning, *Phys. Rev. D* 111 (2) (2025) 022003. [arXiv:2406.06319](#), [doi:10.1103/PhysRevD.111.022003](#).
- [5] D. Bergman, Telescope Array: Latest Results and Expansion Plans, *J. Phys. Conf. Ser.* 1468 (1) (2020) 012078. [doi:10.1088/1742-6596/1468/1/012078](#).
- [6] A. Aab, et al., Depth of maximum of air-shower profiles at the Pierre Auger Observatory. II. Composition implications, *Phys. Rev. D* 90 (12) (2014) 122006. [arXiv:1409.5083](#), [doi:10.1103/PhysRevD.90.122006](#).
- [7] M. De Domenico, M. Settimo, S. Riggi, E. Bertin, Reinterpreting the development of extensive air showers initiated by nuclei and photons, *JCAP* 07 (2013) 050. [arXiv:1305.2331](#), [doi:10.1088/1475-7516/2013/07/050](#).
- [8] L. B. Arbeletche, V. de Souza, On the parametrization of the distributions of depth of shower maximum of ultra-high energy extensive air showers, *Astropart. Phys.* 116 (2020) 102389. [arXiv:1903.03174](#), [doi:10.1016/j.astropartphys.2019.102389](#).
- [9] F. Riehn, R. Engel, A. Fedynitch, T. K. Gaisser, T. Stanev, Hadronic interaction model Sibyll 2.3d and extensive air showers, *Phys. Rev. D* 102 (6) (2020) 063002. [arXiv:1912.03300](#), [doi:10.1103/PhysRevD.102.063002](#).
- [10] T. Pierog, K. Werner, EPOS LHC-R : up-to-date hadronic model for EAS simulations, *PoS ICRC2023* (2023) 230. [doi:10.22323/1.444.0230](#).
- [11] S. Ostapchenko, QGSJET-III model of high energy hadronic interactions. II. Particle production and extensive air shower characteristics, *Phys. Rev. D* 109 (9) (2024) 094019. [arXiv:2403.16106](#), [doi:10.1103/PhysRevD.109.094019](#).

- [12] J. Matthews, A Heitler model of extensive air showers, *Astropart. Phys.* 22 (2005) 387–397. [doi:10.1016/j.astropartphys.2004.09.003](https://doi.org/10.1016/j.astropartphys.2004.09.003).
- [13] S. Mollerach, E. Roulet, Impact of the EPOS.LHC-R hadronic interaction model on the Centaurus A ultrahigh-energy cosmic-ray scenario (12 2025). [arXiv:2512.21415](https://arxiv.org/abs/2512.21415).
- [14] H. Dembinski, P. O. et al., scikit-hep/iminuit, <https://doi.org/10.5281/zenodo.3949207> (Dec 2020). [doi:10.5281/zenodo.3949207](https://doi.org/10.5281/zenodo.3949207).
- [15] A. Aab, et al., Combined fit of spectrum and composition data as measured by the Pierre Auger Observatory, *JCAP* 04 (2017) 038, [Erratum: *JCAP* 03, E02 (2018)]. [arXiv:1612.07155](https://arxiv.org/abs/1612.07155), [doi:10.1088/1475-7516/2017/04/038](https://doi.org/10.1088/1475-7516/2017/04/038).
- [16] A. Abdul Halim, et al., Impact of the magnetic horizon on the interpretation of the Pierre Auger Observatory spectrum and composition data, *JCAP* 07 (2024) 094. [arXiv:2404.03533](https://arxiv.org/abs/2404.03533), [doi:10.1088/1475-7516/2024/07/094](https://doi.org/10.1088/1475-7516/2024/07/094).
- [17] C. Evoli, Fit coefficients for X_{\max} mean and variance parameterisations (SIBYLL/EPOS/QGSJet) (Feb. 2026). [doi:10.5281/zenodo.18710120](https://doi.org/10.5281/zenodo.18710120).

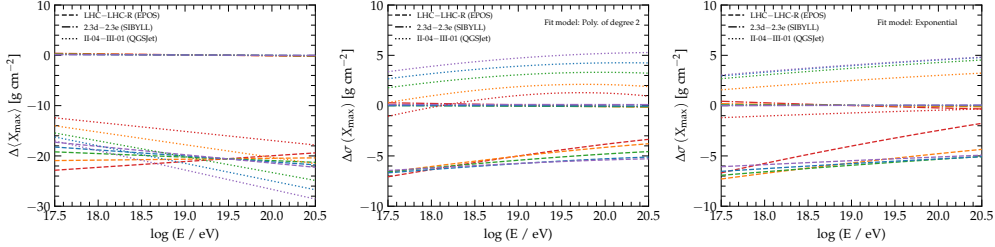


Figure A.10: Absolute differences between the X_{\max} moment parametrizations derived with the updated hadronic interaction models and those obtained with the corresponding earlier versions. Shown are the shifts in $\langle X_{\max} \rangle$ (left) and in $\sigma(X_{\max}) = \sqrt{\sigma^2(X_{\max})}$ using the polynomial (pol2) variance model (center) and the exponential (exp) variance model (right), as a function of energy. Curves compare EPOS-LHC-R to EPOS-LHC, Sibyll 2.3e to Sibyll 2.3d, and QGSJet III-01 to QGSJet II-04.

Appendix A. Comparison with previous HIM versions

This work updates earlier X_{\max} moment parametrizations by adopting the most recent implementations of the HIMs used to generate the reference air-shower predictions. To ensure continuity with existing UHECR composition analyses—and to facilitate comparisons with results based on earlier parametrizations—we present here a direct, like-for-like comparison with the parametrizations obtained using the previous HIM versions: EPOS-LHC, Sibyll 2.3d, and QGSJet II-04, which are superseded in this work by EPOS-LHC-R, Sibyll 2.3e, and QGSJet III-01, respectively.

The comparison is performed using the same functional forms, energy binning, and fitting strategy as in the updated analysis, so that differences can be attributed primarily to the HIM updates. To this aim, we produced a dedicated set of CONEX simulations with the earlier HIM versions, using a comparable number of showers and the same energy range as in the updated production.

The best-fit parameters obtained with the earlier HIM versions are reported in Table B.2. A direct comparison between updated and previous parametrizations is shown in Fig. A.10, which reports the absolute differences in $\langle X_{\max} \rangle$ (left) and in $\sigma(X_{\max})$, for both the polynomial (pol2) and exponential (exp) variance models introduced in Section 3. These differences quantify the net impact of the hadronic-model updates on the parametrized X_{\max} response over the past few years.

Overall, Sibyll exhibits the smallest changes: both the mean and the dispersion remain consistent with the previous parametrization within $\lesssim \text{g cm}^{-2}$ over the full energy range considered. In contrast, EPOS and QGSJet show more pronounced updates. For EPOS and QGSJet, the updated parametrization predicts systematically deeper $\langle X_{\max} \rangle$ by up to $\mathcal{O}(10)\text{--}\mathcal{O}(30) \text{ g cm}^{-2}$ (depending on energy), accompanied by a measurable change in the elongation rate at the level of $\sim 10\%$. For the dispersion, QGSJet tends to yield a smaller $\sigma(X_{\max})$, while EPOS shows an increased $\sigma(X_{\max})$, with typical differences reaching up to $\sim 5 \text{ g cm}^{-2}$. Such shifts, can propagate to inferences of $\sigma^2(\ln A)$ and therefore remain relevant for precision composition studies.

Appendix B. Tables

		EPOS LHC-R	Sibyll 2.3e	QGSJet III-01
μ_X	a_0	826.81 ± 0.11	816.44 ± 0.11	804.41 ± 0.10
	a_1	53.53 ± 0.12	56.93 ± 0.11	55.51 ± 0.11
	b_0	-24.51 ± 0.03	-25.82 ± 0.03	-21.89 ± 0.03
	b_1	1.42 ± 0.04	0.75 ± 0.03	0.94 ± 0.03
	$\tilde{\chi}^2$	33.03	9.97	17.23
σ_X^2 (pol2)	c_0	3723 ± 13	3612 ± 13	3431 ± 12
	c_1	-555 ± 10	-552 ± 10	-497 ± 9
	c_2	91 ± 8	47 ± 8	93 ± 7
	d_0	$-4.02\text{e-}01 \pm 1.1\text{e-}03$	$-3.78\text{e-}01 \pm 1.2\text{e-}03$	$-4.02\text{e-}01 \pm 9.9\text{e-}04$
	d_1	$1.12\text{e-}04 \pm 1.7\text{e-}04$	$5.49\text{e-}04 \pm 1.6\text{e-}04$	$-9.41\text{e-}04 \pm 1.1\text{e-}04$
	d_2	$4.71\text{e-}02 \pm 2.7\text{e-}04$	$4.08\text{e-}02 \pm 2.9\text{e-}04$	$4.41\text{e-}02 \pm 2.4\text{e-}04$
	$\tilde{\chi}^2$	26.67	18.14	7.13
σ_X^2 (exp)	f_0	8.263 ± 0.003	8.245 ± 0.003	8.239 ± 0.003
	f_1	-0.143 ± 0.003	-0.146 ± 0.003	-0.128 ± 0.003
	g_0	-0.503 ± 0.001	-0.501 ± 0.001	-0.589 ± 0.001
	g_1	$-2.30\text{e-}04 \pm 1.22\text{e-}03$	$3.94\text{e-}04 \pm 1.19\text{e-}03$	$-1.20\text{e-}02 \pm 1.18\text{e-}03$
	$\tilde{\chi}^2$	12.21	7.48	22.85

Table B.1: Best-fit parameters for the μ_X parametrization (Eq. 4) and for the $\sigma^2(X_{\max})$ parametrizations corresponding to the second-order polynomial model (pol2, Eq. 5) and the exponential model (exp, Eq. 6), obtained from CONEX simulations for the three hadronic interaction models discussed in the main text EPOS LHC-R, Sibyll 2.3e, and QGSJet III-01. The last column reports the reduced χ^2 . Parameters a_0 , a_1 , b_0 , and b_1 are given in g cm^{-2} , whereas c_0 , c_1 , and c_2 are in $\text{g}^2 \text{cm}^{-4}$; all remaining parameters are dimensionless.

		EPOS LHC	Sibyll 2.3d	QGSJet II-04
μ_X	a_0	805.69 ± 0.10	816.54 ± 0.11	789.28 ± 0.11
	a_1	54.68 ± 0.10	56.73 ± 0.11	53.71 ± 0.11
	b_0	-24.18 ± 0.03	-25.83 ± 0.03	-23.80 ± 0.03
	b_1	0.72 ± 0.03	0.79 ± 0.03	0.43 ± 0.03
	$\tilde{\chi}^2$	23.12	8.51	8.36
σ_X^2 (pol2)	c_0	3137 ± 11	3621 ± 13	3550 ± 13
	c_1	-367 ± 8	-569 ± 10	-416 ± 9
	c_2	65 ± 7	49 ± 8	32 ± 7
	d_0	$-4.35e-01 \pm 8.5e-04$	$-3.80e-01 \pm 1.2e-03$	$-3.77e-01 \pm 1.2e-03$
	d_1	$-7.19e-04 \pm 1.1e-04$	$7.19e-04 \pm 1.6e-04$	$1.01e-03 \pm 1.7e-04$
	d_2	$5.22e-02 \pm 2.1e-04$	$4.14e-02 \pm 2.9e-04$	$4.12e-02 \pm 3.0e-04$
	$\tilde{\chi}^2$	24.83	19.26	9.13
σ_X^2 (exp)	f_0	8.129 ± 0.003	8.245 ± 0.003	8.215 ± 0.003
	f_1	-0.097 ± 0.003	-0.154 ± 0.003	-0.120 ± 0.003
	g_0	-0.608 ± 0.001	-0.500 ± 0.001	-0.486 ± 0.001
	g_1	$-1.21e-02 \pm 1.23e-03$	$2.95e-03 \pm 1.19e-03$	$6.60e-03 \pm 1.20e-03$
	$\tilde{\chi}^2$	7.22	6.46	4.04

Table B.2: Best-fit parameters for the μ_X parametrization (Eq. 4) and for the $\sigma^2(X_{\max})$ parametrizations corresponding to the second-order polynomial model (pol2, Eq. 5) and the exponential model (exp, Eq. 6), obtained from CONEX simulations for the earlier version of the three hadronic interaction models discussed in the main text: EPOS LHC, Sibyll 2.3e, and QGSJet II-04. The last column reports the reduced χ^2 . Parameters a_0 , a_1 , b_0 , and b_1 are given in g cm^{-2} , whereas c_0 , c_1 , and c_2 are in $\text{g}^2 \text{cm}^{-4}$; all remaining parameters are dimensionless.

HIM	H	He	N	Si	Fe
EPOS LHC-R	2.05	1.03	1.05	1.44	1.45
Sibyll 2.3e	1.46	0.77	0.52	0.53	0.75
QGSJet III-01	1.83	0.61	1.02	0.66	0.67

Table B.3: Average residuals between the CONEX simulations and the analytical parametrizations for μ_X , computed for each primary species and hadronic interaction model in the energy range $E \gtrsim 10^{17.5}$ eV. Values are expressed in g cm^{-2} .

HIM		H	He	N	Si	Fe
EPOS LHC-R	pol2	2.19	1.78	0.38	0.91	0.38
	exp	1.31	0.92	0.68	0.28	0.40
Sibyll 2.3e	pol2	1.67	1.75	0.43	0.35	0.18
	exp	0.63	0.64	0.77	0.22	0.24
QGSJet III-01	pol2	1.03	0.95	0.27	0.17	0.14
	exp	1.60	1.01	1.24	0.24	0.53

Table B.4: Average residuals between the CONEX simulations and the analytical parametrizations for $\sigma(X_{\max})$, computed for each primary species and hadronic interaction model in the energy range $E \gtrsim 10^{17.5}$ eV and for the two parametrizations proposed in Eqs. (5) (2nd) and (6) (exp). Values are expressed in g cm^{-2} .

	EPOS LHC-R			Sibyll 2.3e			QGSJet III-01		
p_0^μ	796.26	-12.23	-1.55	786.20	-15.99	-1.03	770.84	-8.69	-1.50
p_1^μ	58.67	-0.85	0.29	59.62	0.22	0.02	57.22	0.68	-0.05
p_2^μ	-1.418	-0.172	-0.009	-1.132	0.472	-0.116	-0.084	0.368	-0.153
p_0^σ	43.413	-0.243	-0.830	40.417	-1.956	-0.427	33.632	3.985	-1.276
p_1^σ	3.348	-1.731	0.067	-1.207	-0.238	0.094	-0.289	-3.100	0.427
p_0^λ	0.857	0.406	-0.025	0.793	0.231	0.003	0.651	0.238	0.087
p_1^λ	0.161	0.093	-0.037	0.036	0.025	-0.001	0.047	-0.026	-0.032

Table B.5: Best-fit coefficients of the generalized Gumbel parameterization of the X_{\max} distributions for the three hadronic interaction models EPOS LHC-R, Sibyll 2.3e, and QGSJet III-01, obtained from a global unbinned maximum-likelihood fit to CONEX simulations. For each model, the three entries in a row correspond to the coefficients of the quadratic dependence on $Y = \ln A$ defining $p_j(Y) = a_j + b_j Y + c_j Y^2$ (see Eqs. (21)–(23)).